Structural Optimization of 3D Porous Electrodes for High-Rate Performance Lithium Ion Batteries

Jianchao Ye,* Andreas C. Baumgaertel, Y. Morris Wang, Juergen Biener, and Monika M. Biener*

Nanoscale Synthesis and Characterization Laboratory, Lawrence Livermore National Laboratory, 7000 East Avenue, Livermore, California 94550, United States

ABSTRACT Much progress has recently been made in the development of active materials, electrode morphologies and electrolytes for lithium ion batteries. Well-defined studies on size effects of the three-dimensional (3D) electrode architecture, however, remain to be rare due to the lack of suitable material platforms where the critical length scales (such as pore size and thickness of the active material) can be freely and deterministically adjusted over a wide range without affecting the overall 3D morphology of the electrode. Here, we report on a systematic study on length scale effects on the electrochemical performance of model 3D np-Au/TiO_2 core/shell electrodes. Bulk nanoporous gold provides deterministic control over the pore size and is used as a monolithic metallic scaffold and current collector. Extremely uniform and conformal TiO_2 films of controlled thickness were deposited on the current collector by employing atomic layer deposition (ALD). Our experiments demonstrate profound performance improvements by matching the Li^+ diffusivity in the electrolyte and the solid state through adjusting pore size and thickness of the active coating which, for 200 μm thick porous electrodes, requires the presence of 100 nm pores. Decreasing the thickness of the TiO_2 coating generally improves the power performance of the electrode by reducing the Li^+ diffusion pathway, enhancing the Li^+ solid solubility, and minimizing the voltage drop across the electrode/electrolyte interface. With the use of the optimized electrode morphology, supercapacitor-like power performance with lithium-ion-battery energy densities was realized. Our results provide the much-needed fundamental insight for the rational design of the 3D architecture of lithium ion battery electrodes with improved power performance.

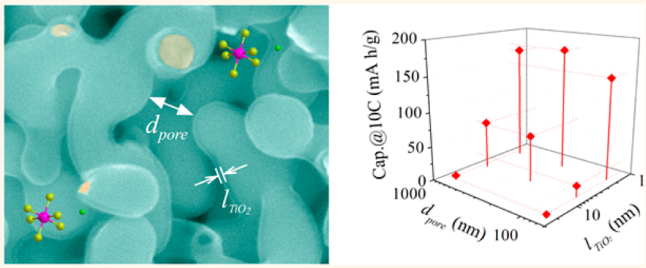

KEYWORDS: Atomic layer deposition · nanoporous gold · TiO_2 · lithium ion batteries · length scales

Today's lithium ion battery (LIB) development is driven by the desire to increase the energy and power densities (per volume and footprint), lifetime, and making LIBs inherently safe.[1,2] The performance of LIB electrodes is generally governed by the thermodynamics and kinetics of several interconnected processes, including Li^+ diffusion/migration in the electrolyte through interconnected pores, charge transfer at the electrolyte/electrode interface, Li^+ transportation/storage and electron transport in the active material of the electrode (Figure 1a).[3] All these processes have in common that they are strongly affected by the structural design of the electrode, specially the length scales involved in both the active material and the porous network. However, despite the obvious importance for rational electrode design, surprisingly little is known about the fundamental relationships between Li^+ storage behavior and the three-dimensional (3D) architecture of the electrode as the majority of efforts have been focused on the geometrical and physical design of the active material alone.[4−9] Furthermore, most current LIB designs are particle based and require the use of conductive additives and binders. These conventional electrode preparation methods provide little control over the porous structure, which makes it difficult to separate the intrinsic electrochemical properties of the active material from size effects related to the overall electrode architecture.

An example of a commonly accepted architectural design rule is that the presence of large pores facilitates electrolyte-based ion mass transport in porous materials, and thus positively affects the gravimetric power density. We were thus surprised by our

* Address correspondence to ye3@llnl.gov, biener3@llnl.gov.

Received for review September 27, 2014 and accepted December 9, 2014.

Published online December 09, 2014
10.1021/nn505490u

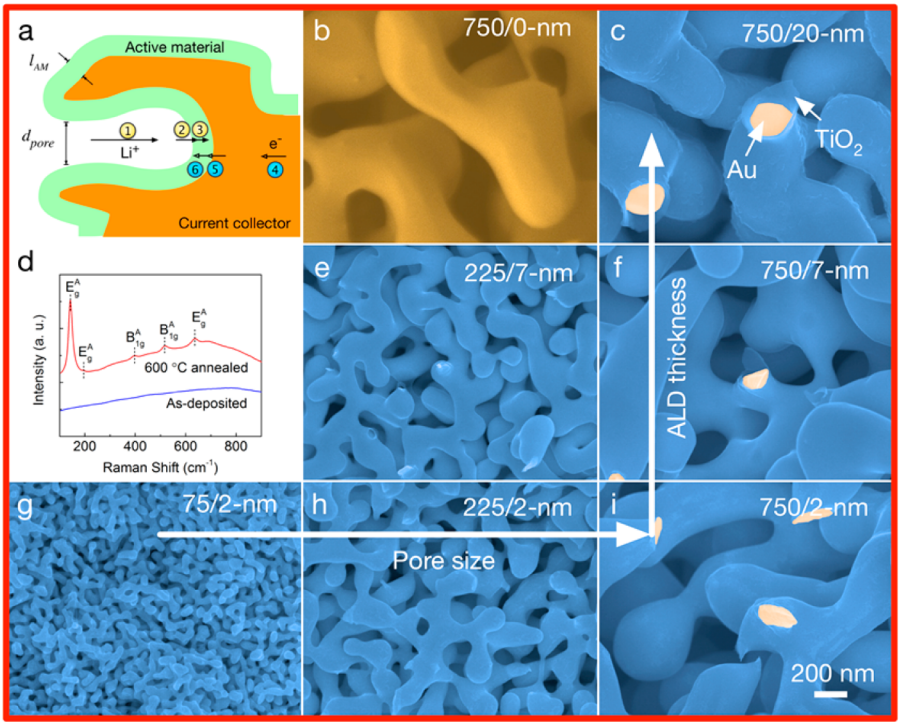

Figure 1. Relevant transport processes and microstructure of 3D np-Au/TiO_2 electrodes for lithium ion batteries. (a) An illustration of relevant transport processes in 3D porous LIB electrodes: (1) Li^+ transport through the electrolyte; (2) charge transfer at the electrolyte/electrode interface; (3) Li^+ transport in the active material; (4) electron transport in the current collector; (5) electron transfer from the current collector to the active material; (6) Li^+/electron recombination. (b) Scanning electron micrograph (SEM) of np-Au with a pore size of 750 nm. (c, e−i) SEM images of TiO_2 ALD coated np-Au samples after annealing at 600 °C for various pore size (75, 225, and 750 nm) and TiO_2 film thickness (2, 7, and 20 nm). All SEM images were taken at the same magnification. (d) Raman spectra from a TiO_2-coated np-Au sample measured before and after annealing at 600 °C revealing the phase transition from as-deposited amorphous TiO_2 to anatase.

recent findings that the gravimetric power density of graphene-based supercapacitor electrodes is only marginally affected by 8-fold compression of the porous electrode material, which completely removed the macroporosity and part of the mesoporosity.[10] This result demonstrates the importance of better design rules for porous electrodes. In this work, we systematically studied length scale effects in the context of electrode performance of LIBs. To achieve this goal, we employed a monolithic LIB electrode design that provides deterministic control over pore size and thickness of the active material. The use of conductive additives and binders is avoided by using monolithic nanoporous gold (np-Au) as scaffold and current collector. Deterministic control over the thickness of the active material, TiO_2, is achieved by employing atomic layer deposition (ALD).

Nanoporous gold has a unique bicontinuous microstructure consisting of two interpenetrating networks of nanoscale ligaments and pores thus providing continuous pathways for both ions and electrons (Figure 1b). The material has a unimodal pore/ligament size distribution that can be tuned, without changing the porosity or connectivity of the ligament/pore system, in the range from ~50 nm to 3 μm by a simple annealing procedure.[11] The monolithic structure of bulk np-Au provides fast electron transport thus minimizing the voltage drop (commonly referred to as the IR drop) in the current collector. For the same reason, ultrathin (100 nm thick) np-Au films have been previously used by other groups as current collector for supercapacitors and LIB electrodes.[12] These ultrathin films, however, are not suitable for length scale studies as the 3D structure of np-Au collapses into a 2D film as the pore size approaches the film thickness.[13] By contrast, the np-Au bulk materials used in the present study are 200-μm thick and can thus accommodate micron-sized pores. The thickness of our electrodes is commensurate with commercial electrode designs, and our results thus have direct practical implications.[14] Although the cost of gold is too high for practical battery applications, we decided to use nanoporous gold for the present model study because its chemical inertness leads to better length scale control compared to other nanoporous metal systems generated by dealloying. The design rules developed in this study, however, are directly transferable to other nanoporous current collectors, such as 3D graphene and less expensive metal foams (*e.g.*, Cu, Ni, and Al).[15−26]

Unlike previous electroless plating approaches,[27] ALD allows one to coat ultrahigh aspect ratio

substrates such as np-Au with uniform and conformal films with atom-scale thickness control by employing alternating self-limiting surface reactions. Consequently, ALD is considered to be a key technology in the energy-storage field.[28] Successful applications include, for example, surface modifications and direct synthesis of active materials for lithium ion batteries.[29−32] Here, we use the ALD process to coat the np-Au current collector with conformal TiO_2 films (Figure 1c,e−i). We previously developed and characterized such monolithic np-Au/metal oxide core/shell composite materials for catalytic applications where they showed excellent performance and stability.[33] As an environmentally friendly material with abundant resources on earth, TiO_2 is also an attractive anode candidate for LIBs due to its cycling stability and safety. Many studies[34−39] on particle-based or composite TiO_2 electrodes have attempted to identify size/geometry effects on the Li^+ storage capability, but such electrode systems often suffer from poor control over the overall porous structure, nanoparticle aggregation, not well-defined electrode/electrolyte interfaces, poor contact between active material and current collector, and poor mechanical stability. By contrast, the core/shell architecture of the monolithic 3D ALD TiO_2/np-Au electrodes used in the present study is well-defined and mechanically robust,[40] and provides a stable interface between the np-Au current collector and the active material for good electrical contact.

RESULTS AND DISCUSSION

Figure 1(c,e−i) shows SEM images of a set of TiO_2 ALD coated np-Au samples with three different pores sizes (75, 225, and 750 nm) and three different TiO_2 coating thicknesses (2, 7, and 20 nm) after annealing in air at 600 °C for 1 h. For simplicity, samples will be denoted as *d*/*l*-nm TiO_2 in the following sections, where *d* denotes the pore size and *l* is the ALD film thickness. The pore size was adjusted by annealing the uncoated np-Au samples in air (300−500 °C), and the thickness of the TiO_2 coatings was adjusted by the number of ALD cycles applied (30−300 cycles). In all cases, the np-Au ligaments are coated with uniform and conformal TiO_2 films. Consistent with our previous work using X-ray adsorption spectroscopy,[33] Raman spectra (Figure 1d) reveal that the postdeposition annealing procedure at 600 °C triggers a phase transition from as-deposited amorphous to anatase. As a side note, standard XRD analysis does not detect the presence of only 2 nm thick TiO2 films on np-Au.[33]

This set of samples was then used for electrochemical characterization to systematically study length scale effects in 3D LIB electrodes. Galvanostatic charge/discharge experiments were carried out in a half-cell setup with a lithium chip as the counter electrode (Figure 2a, for details see Methods). The cells were initially run at 1C rate (1C equals 168 mAh/g) for

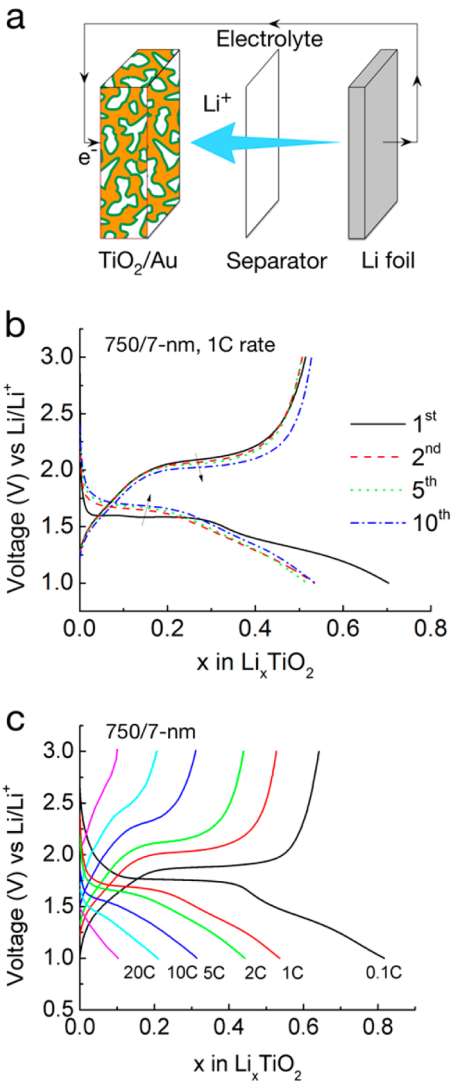

Figure 2. Experimental setup and galvanostatic charge/discharge plots. (a) The schematic of the two-electrode setup for galvanostatic charge/discharge experiments using a lithium chip as the counter electrode; (b) Voltage profiles collected from 750/7-nm anatase samples during the first 10 cycles at 1C rate; (c) voltage profiles of the 750/7-nm anatase sample obtained from rate jump experiments (0.1C to 20C, 1C equals 168 mA/g current density). The curves were taken from the last cycle at each rate.

10 cycles to stabilize the performance. Figure 2b shows the first ten charge/discharge voltage profiles collected from a 750/7-nm sample. The first discharge (Li^+ insertion into TiO_2) results in a capacity of 236 mAh/g (0.70 Li per TiO_2), of which 63 mAh/g (0.19 Li per TiO_2) is irreversible. The reversible capacity of 173 mAh/g corresponds to a composition of $Li_{0.51}TiO_2$, consistent with the value of 168 mAh/g reported in previous experimental and theoretical studies for the Li^+ storage capability of anatase TiO_2.[36,41] The origin of the irreversible capacity observed in the present study is not clear, but similar observations have been reported previously and attributed to the trapping of Li^+ in defect sites with high binding energies,[42,43] surface absorbed water molecules,[43,44] or solid electrolyte

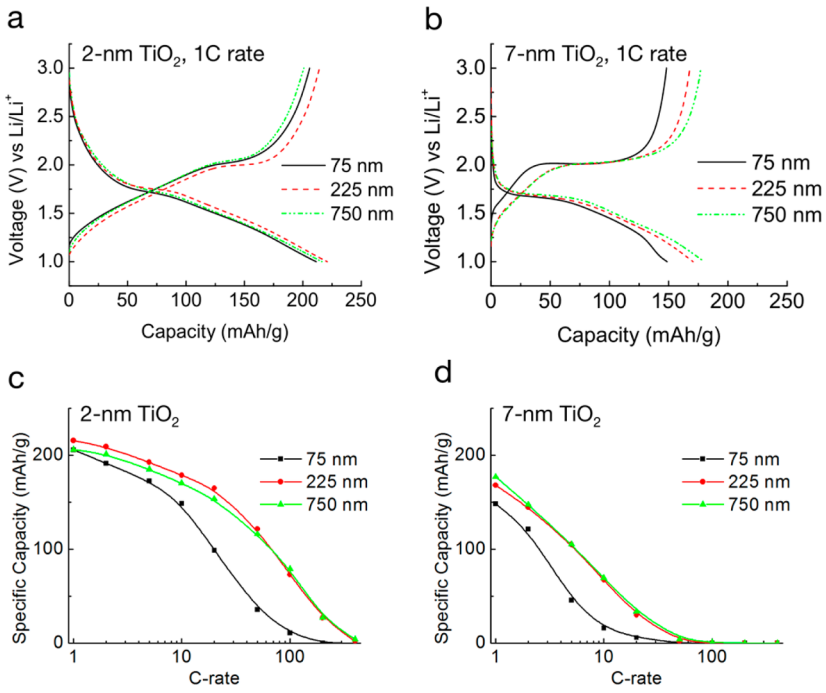

Figure 3. Effect of pore size, TiO_2 layer thickness, and cycling rate on the specific capacity of np-Au/TiO_2 electrodes. (a) For 2 nm thick TiO_2 films and low rates (1C), the pore size has little effect on the measured voltage profiles; Significant reduction of the specific capacity was observed for small pore size (75 nm)/thicker TiO_2 film (7 nm) combinations (b) and/or higher-rate cycling (c and d).

interface (SEI) formation.[45,46] The reduction/oxidation plateaus, occurring at around 1.7 and 2.0 V, respectively, are indicative of a two-phase reaction mechanism in anatase TiO_2 (from tetragonal to orthorhombic and *vice versa*).[36] The voltage gap between the reduction/oxidation plateaus narrows slightly during the first 10 cycles. The Coulombic efficiency also improves, from 73.2% in the first cycle to 95.3% in the second cycle and 98.8% in the 10th cycle. Rate jump experiments were then carried out in the rate range of 1−400C (1C = 168 mA/g, 400C = 67 A/g) to study the detailed kinetics. The raw data of charge/discharge capacities at varied C-rates can be found in Figure S1, Supporting Information, and typical voltage profiles for the 750/7-nm TiO_2 sample are shown in Figure 2c. With increasing charge/discharge rate, the potential separation between the redox peaks increases and the capacity decreases indicating polarization losses (IR drop) caused by rate limiting charge transport either in solid TiO_2 or liquid electrolyte.

To identify the rate-limiting processes, we systematically studied the rate performance as a function of both pore size and TiO_2 film thickness. The effects of pore size on the voltage profiles and rate performance are summarized in Figure 3. For 2 nm thick anatase TiO_2 samples, the voltage profiles measured at 1C rate are independent of the pore size (Figure 3a). This demonstrates that, at 1C rate, Li^+ ion transport through the electrolyte is always fast enough to keep up with the Li^+ uptake of the 2 nm thick TiO_2 coating. For higher rates, however, the performance improves drastically with increasing pore size from 75 to 225 nm (Figure 3c). For example, at 50C rate, the capacity of the 2 nm TiO_2 increases by 300%, from 30 mAh/g (75 nm pores) to 120 mAh/g (225 nm pores). This improvement in rate performance is also observed for 7 nm thick TiO_2 films (Figure 3b, d). For these thicker TiO_2 coatings, an increase in capacity with increasing pore size from 75 to 225 nm was even observed at rates as low as 1C (Figure 3b). No further capacity gain is observed by further increasing the pores to 750 nm, implying that a pore size of 225 nm or above provides sufficiently fast Li^+ transport through the electrolyte to keep up with the Li^+ uptake of a 7 nm thick TiO_2 film. This is true at least for the ultrathick electrodes we studied here. On the other hand, at rates higher than 1C, a pore size of 75 nm or below will limit Li^+ supply to TiO_2 with a thickness of 2 nm or above. This critical pore size between 75 and 225 nm is surprisingly high for the design of porous electrodes.

A small fraction of the pronounced rate performance changes observed in Figure 3 can be attributed to the fact that the porosity of the np-Au/TiO_2 composite material decreases with increasing TiO_2 film thickness which effectively reduces the Li^+ diffusivity in the nanoporous electrode. The effective Li^+ diffusivity through the electrolyte in 3D np-Au/TiO_2 electrodes can be described as $D_e = D\varepsilon_t/\tau$.[47−49] Here, D is the diffusion coefficient in the absence of a porous media; ε_t is the porosity available for the transport that equals to the total porosity of 0.7 for np-Au; τ is the tortuosity (a tortuosity value of 3.2 ± 0.2 has recently been

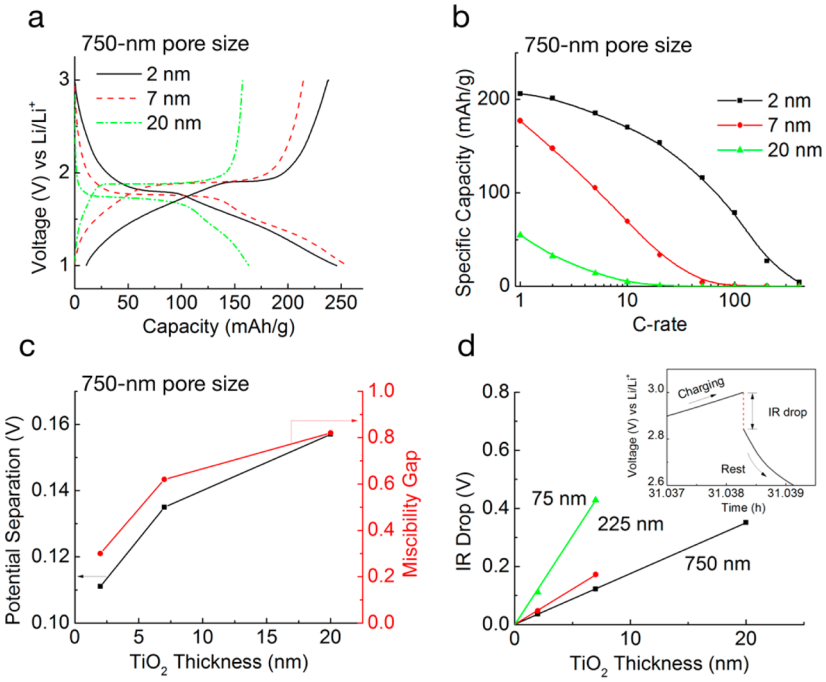

Figure 4. Effect of the TiO_2 layer thickness on (a) charge/discharge voltage profiles (measured at 0.1C) and (b) the rate performance of np-Au/TiO_2 electrodes with 750 nm pores. (c) Potential separation and miscibility gap measured at 0.1C as a function of the TiO_2 layer thickness. (d) IR drop/TiO_2 layer thickness dependency for various pore sizes measured by the current interrupt method. The inset shows a typical charge-rest-discharge voltage profile collected from a 750/7-nm sample (charge/discharge at 10C, interrupted at 3 V). Note the linear correlation between IR drop and TiO_2 layer thickness.

reported for np-Au[50]). As annealing induced coarsening of np-Au does not change the porosity or the connectivity of the ligaments, we assume that the tortuosity of np-Au is independent of the length scale of the structure. Thick ALD coatings, however, will reduce the porosity of np-Au and thus also increase the tortuosity as porosity and tortuosity are correlated with each other through the generalized Bruggeman relation,[49] $\tau = \varepsilon_t^{-\alpha}$, where the Bruggeman exponent α is ~3 for np-Au (based on the tortuosity/porosity combination of 3.2/0.7). Thin ALD coatings (2 nm) cause only small changes in porosity (up to 4% for 75/2-nm samples), but the presence of thicker films can lead to more pronounced changes in porosity (*e.g.*, 17% for 75/7-nm samples). Thus, while some of the rate performance changes of the thicker coatings (Figure 3d) may be attributed to porosity and the correlated tortuosity changes, this cannot explain the large changes observed for thin coatings (Figure 3c). Those may reflect contributions from the ionic resistance of the electrolyte as the volumetric mass of the active material increases with decreasing pore size thus requiring higher currents for a given *C* rate. This can lead to polarization effects (IR drop) which will be discussed in detail below.

To better differentiate between ALD induced porosity changes and other TiO_2 film thickness effects we studied a set of large pore samples (750/*x*-nm) where porosity changes can be neglected even for thick coatings (4% porosity change for the 750/20-nm sample) (Figure 4). At a low rate of 0.1C, decreasing the TiO_2 layer thickness in 750 nm pore material, from 20 to 7 and 2 nm, increases the capacity from 157 to 214 and 227 mAh/g, respectively. This performance improvement becomes even more pronounced at higher rates as shown in Figure 4b. The thermodynamic and kinetic improvement of the Li^+ storage capability with decreasing TiO_2 layer thickness can be attributed to narrowing of the potential gap between the reduction and oxidation peaks (from 0.16 to 0.11 V), and a decreasing miscibility gap[36,37] (portion of the plateau, from 82% to 30%), as shown in Figure 4c. Decreasing the TiO_2 layer thickness reduces the Li^+ solid state diffusion length thus minimizing performance limitations arising from slow Li^+ diffusion in solid TiO_2. The nanoscale architecture of our core/shell material also increases the fraction of Li^+ storage sites in the surface region and enhances the Li^+ solid solubility in TiO_2,[36,37] especially for samples with a TiO_2 layer thickness of only 2 nm. As a result, the two-phase reaction in bulk TiO_2 is partially replaced with single-phase reaction in nanosized TiO_2, which decreases the length of the plateau, that is, the miscibility gap. With the absence of a Li-rich/Li-poor phase boundary, the phase transition induced barrier that impedes the Li^+ transportation process is greatly reduced,[51] which could explain the observed narrowing of the potential gap.

In the following, we further analyze the length scale dependence of the IR drop on the thickness of TiO_2

layer. This allows us to differentiate between contributions arising from the electronic/ionic resistance of TiO_2 (R_{TiO_2}), and contributions coming from the ionic resistance of the electrolyte R_e and the electrode–electrolyte interfacial resistance (R_i). Electronic transport limitations related to the np-Au current collector can be ruled out due to the high electronic conductivity of gold and the continuous ligament morphology. The IR drop ΔV_{TiO_2} due to the resistance of the TiO_2 layer can be expressed as

$$\Delta V_{TiO_2} = IR_{TiO_2} \approx I_c \cdot \rho \cdot d_{TiO_2} \cdot l_{TiO_2}^2 \quad (1)$$

where I_c is the current density at a certain C-rate (*i.e.*, I_c = 1680 mA/g at 10C rate), ρ is the electronic/ionic resistivity of the TiO_2 layer (anatase: $\sim 10^6$ ohm·cm[52]), d_{TiO_2} is the volumetric density of TiO_2 (anatase: 3.79 g/cm^3[3,53]), and l_{TiO_2} is the thickness of TiO_2 layer. Equation 1 suggests that ΔV_{TiO_2} scales quadratically with the TiO_2 thickness. The *IR* drop ΔV_{EI} due to R_e and R_i, both of which are independent of the TiO_2 thickness, can be expressed as

$$\Delta V_{EI} = I(R_e + R_i) \approx I_c \cdot d_{TiO_2} \cdot S \cdot (R_e + R_i) \cdot l_{TiO_2} \quad (2)$$

where S is the surface area of the 3D porous electrode, which is inverse proportional to the pore size of the 3D electrode. For a given pore size and C-rate, ΔV_{EI} is thus linearly proportional to the TiO_2 film thickness. Here, we use the current interrupt method to measure the overall IR drop of the system.[54] Specifically, we performed galvanostatic charge/discharge experiments at a rate of 10C while switching off the charging current at 3 V. The immediate cell voltage decay response provides a measure for the overall IR drop of the system (Figure 4d, inset). The observed linear relationship of the IR drop with the TiO_2 film thickness (Figure 4d) reveals that charge transport is limited by the electrolyte and the electrode/electrolyte interface (ΔV_{EI}) and not by the electronic/ionic resistance of the TiO_2 layer (ΔV_{TiO_2}) that would lead to an IR drop that scales quadratically with the TiO_2 film thickness. It has been recognized that the resistance of the active material is an important factor that can inhibit the high power output of batteries.[25] While this conclusion may be true for microstructured electrodes, our finding suggests that electron transport limitations can be overcome by using optimized nanoscale architectures. The IR drop caused by the electrolyte and the interface forces the cell potential to go earlier beyond the charge/discharge voltage window (1–3 V) and thus results in a lower capacity, especially at very high C-rates. The correlation between capacity and IR drop is shown in Figure S2, Supporting Information.

Finally, the effect of pore size and TiO_2 film thickness on the energy and power density performance of 3D np-Au/TiO_2 electrodes is summarized using a Ragone plot (Figure 5). At low charge/discharge rates, the

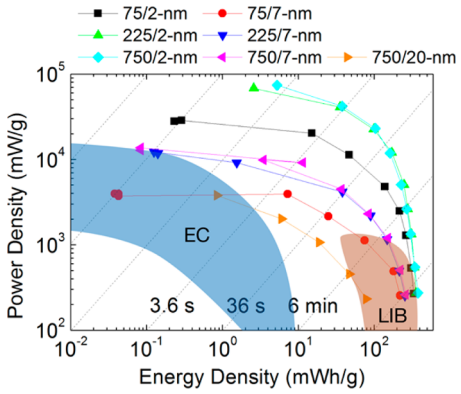

Figure 5. Ragone plot for 3D np-Au/TiO_2 electrodes. For comparison, the typical characteristics of electrochemical capacitors (EC, blue shadow region) and lithium ion batteries (LIB, brown shadow region) are included.[57,58] Dashed lines denote the discharge time of a half cell.

electrode performance falls into the high-energy density lithium-ion-battery region. With increasing charge/discharge rates, the energy density decreases and approaches values more characteristic for electrochemical supercapacitors. This drop in energy density is especially pronounced for samples with thick ALD films and small pores (*e.g.*, 75/7-nm and 750/20-nm). Li^+ ion storage in these materials under high rate conditions seems to be limited to a thin layer near the surface of the bulk nanoporous electrode thus leading to inefficient utilization of the TiO_2 storage material. However, by using optimized ALD layer thickness/pore size combinations, high gravimetric energy densities can be realized even at supercapacitor-like power densities. For example, the 225/2-nm TiO_2 sample combines a power density of 13 W/g with an energy density of 130 mWh/g at a time scale of only 36 s, indicating a high degree of TiO_2 utilization even at high power. Actually, our ultrathick electrodes outperform even much thinner and doctor blading prepared film electrodes on a pure gravimetric base (Figure S3, Supporting Information). On the other hand, the 75/7-nm TiO_2 sample, at the same time scale, shows the best combination of footprint performance (Figure S4, Supporting Information), with an areal power and energy density of 30 mW/cm^2 and 0.3 mWh/cm^2, respectively. Due to our ultrathick (200 μm) electrode design, the footprint power and energy density is much higher than that of thin electrodes reported previously.[24,32,55,56] Finally, our electrodes are very stable as demonstrated by the long-term cycle test results shown in Figure S5, Supporting Information. The excellent long-term cycling stability with 98.5% capacity retention after 500 charge/discharge cycles can be attributed to the robust core/shell architecture. These results clearly demonstrate the importance of understanding length scale effects in porous electrodes, and developing design rules for the architecture of next generation LIB electrodes.

CONCLUSION

We developed a generic model system for structural optimization of 3D porous LIB electrodes. Specifically, our model system consists of monolithic np-Au as fully tunable nanoporous current collector and scaffold, and conformal TiO_2 ALD coatings with atomic-scale thickness control. The rate performance of these monolithic 3D core/shell electrodes can be significantly improved by matching the kinetics of liquid phase diffusion and solid-state reactions through adjusting pore size and ALD layer thickness. We found that for electrodes with commercially relevant thicknesses (~200 μm), Li^+ transportation through the liquid electrolyte can become rate-limiting for small pore size (75 nm)/high rate combinations. The high-rate performance is dramatically improved by reducing the TiO_2 thickness primarily due to the reduced Li^+ diffusion pathway and enhanced solid solubility. The linear relationship of the IR drop and TiO_2 thickness suggests that electron transport in TiO_2 with a thickness of less than 20 nm is not a rate-limiting process. Instead, the IR drop is dominated by interfacial charge-transfer and electrolyte resistance, which limit Li^+ storage capability at higher rates. Overall, the length-scale design allows mechanistic studies in a systematic way and provides a pathway forward to realize high power densities in thick LIB battery electrodes.

METHODS

Sample Preparation. The $Ag_{70}Au_{30}$ alloy discs with diameter of 5 mm and thickness of 200 μm were immersed in 72 mL concentrated nitric acid at room temperature. The color of the discs changed from silver to brown in just a few seconds. After dealloying for 48 h, the discs were washed with deionized water and dried in air. The weight change of alloys was monitored in order to confirm the complete removal of Ag. The resultant np-Au templates were annealed at 300 and 500 °C in air for 60 min to adjust the pore size from as-dealloyed 75 to 225 and 750 nm, respectively. The active TiO_2 ALD coatings were deposited in a warm wall reactor (wall temperature of 100 °C and stage temperature of 110 °C) on ALD-200L system (Kurt J. Lesker Company) using titanium tetrachloride ($TiCl_4$) as the Ti source and H_2O as the O source. Long pump, exposure, and purge times (20/300/300 s) were used to ensure the gas precursors penetrate through the np-Au discs and achieve uniform coatings. The anatase TiO_2 was obtained by annealing the as-deposited np-Au/TiO_2 electrode at 600 °C in air for 60 min.

Materials Characterization. The morphology of the np-Au/TiO_2 core/shell samples was characterized with a field emission scanning electron microscope (JEOL 7401-F) at 20 keV (20 mA) in secondary electron imaging mode with a working distance of 5−8 mm. The Raman spectra for TiO_2 phase identification were collected using a Nicolet Almega XR dispersive micro-Raman spectrometer with 633 nm excitation length. To avoid crystallization of TiO_2, a low laser beam power (as low as 0.67 mW) and a spot size of 1.3 μm was selected.

Electrochemical characterization. A two-electrode setup was used for galvanostatic charge/discharge experiments. Swagelok type half cells were prepared inside an argon filled glovebox with moisture and oxygen levels below 1 ppm. $LiPF_6$ (1 M) in a 1/1/1 (vol) mixture of ethylene carbonate/diethyl carbonate/dimethyl carbonate (EC/DEC/DMC) (MTI, Cor.) was used as the electrolyte and polypropylene membrane (Celgard 3501) as the separator. A lithium chip with diameter of 9.5 mm and a thickness of 250 μm was placed on the current collector as the counter electrode. A double-layer separator was placed on top of the lithium chip and soaked with electrolyte. Directly after assembly, the cells were rested for at least 5 h. Then, the cells were discharged (Li^+ insertion) and charged (Li^+ extraction) galvanostatically in a potential window between 1 and 3 V at various rates ranging from 1C up to 400C using a Maccor Model 4304 battery tester or a MTI 8 Channel Battery Analyzer. A 5-s rest step was inserted after each charge or discharge step. All electrochemical tests were performed at ambient conditions.

Conflict of Interest: The authors declare no competing financial interest.

Supporting Information Available: Charge/discharge capacities obtained from rate-jump experiments. Correlation between specific capacity and IR drop. Rate performance of 225/2-nm TiO_2 compared to reference data. Footprint power *versus* energy density. Long-term cycling stability of 3D np-Au/TiO_2 electrodes. This material is available free of charge *via* the Internet at http://pubs.acs.org.

Acknowledgment. Work at LLNL was performed under the auspices of the U.S. Department of Energy by LLNL under Contract DE-AC52-07NA27344. Project 13-LWD-031 was funded by the Laboratory Directed Research and Development (LDRD) Program at LLNL.

REFERENCES AND NOTES

1. Simon, P.; Gogotsi, Y.; Dunn, B. Where Do Batteries End and Supercapacitors Begin? *Science* **2014**, *343*, 1210–1211.
2. Naguib, M.; Halim, J.; Lu, J.; Cook, K. M.; Hultman, L.; Gogotsi, Y.; Barsoum, M. W. New Two-Dimensional Niobium and Vanadium Carbides as Promising Materials for Li-Ion Batteries. *J. Am. Chem. Soc.* **2013**, *135*, 15966–15969.
3. Park, M.; Zhang, X. C.; Chung, M. D.; Less, G. B.; Sastry, A. M. A Review of Conduction Phenomena in Li-Ion Batteries. *J. Power Sources* **2010**, *195*, 7904–7929.
4. Etacheri, V.; Yourey, J. E.; Bartlett, B. M. Chemically Bonded TiO_2-Bronze Nanosheet/Reduced Graphene Oxide Hybrid for High-Power Lithium Ion Batteries. *ACS Nano* **2014**, *8*, 1491–1499.
5. Augustyn, V.; Simon, P.; Dunn, B. Pseudocapacitive Oxide Materials for High-Rate Electrochemical Energy Storage. *Energy Environ. Sci.* **2014**, *7*, 1597–1614.
6. Xia, T.; Zhang, W.; Murowchick, J.; Liu, G.; Chen, X. Built-in Electric Field-Assisted Surface-Amorphized Nanocrystals for High-Rate Lithium-Ion Battery. *Nano Lett.* **2013**, *13*, 5289–5296.
7. Myung, S.-T.; Kikuchi, M.; Yoon, C. S.; Yashiro, H.; Kim, S.-J.; Sun, Y.-K.; Scrosati, B. Black Anatase Titania Enabling Ultra High Cycling Rates for Rechargeable Lithium Batteries. *Energy Environ. Sci.* **2013**, *6*, 2609.
8. Li, W.; Wang, F.; Feng, S. S.; Wang, J. X.; Sun, Z. K.; Li, B.; Li, Y. H.; Yang, J. P.; Elzatahry, A. A.; Xia, Y. Y.; *et al.* Sol-Gel Design Strategy for Ultradispersed TiO_2 Nanoparticles on Graphene for High-Performance Lithium Ion Batteries. *J. Am. Chem. Soc.* **2013**, *135*, 18300–18303.
9. Xiong, H.; Yildirim, H.; Shevchenko, E. V.; Prakapenka, V. B.; Koo, B.; Slater, M. D.; Balasubramanian, M.; Sankaranarayanan, S. K. R. S.; Greeley, J. P.; Tepavcevic, S.; *et al.* Self-Improving Anode for Lithium-Ion Batteries Based on Amorphous to Cubic Phase Transition in TiO_2 Nanotubes. *J. Phys. Chem. C* **2012**, *116*, 3181–3187.
10. Merrill, M.; Montalvo, E.; Campbell, P. G.; Wang, Y.; Stadermann, M.; Baumann, T.; Biener, J.; Worsley, M. Optimizing Supercapacitor Electrode Density: Achieving the Energy of Organic Electrolytes with the Power of Aqueous Electrolytes. *RSC Adv.* **2014**, *4*, 42942–42946.

11. Biener, M. M.; Biener, J.; Wichmann, A.; Wittstock, A.; Baumann, T. F.; Baumer, M.; Hamza, A. V. ALD Functionalized Nanoporous Gold: Thermal Stability, Mechanical Properties, and Catalytic Activity. *Nano Lett.* **2011**, *11*, 3085–3090.
12. Lang, X. Y.; Hirata, A.; Fujita, T.; Chen, M. W. Nanoporous Metal/Oxide Hybrid Electrodes for Electrochemical Supercapacitors. *Nat. Nanotechnol.* **2011**, *6*, 232–236.
13. Ding, Y.; Kim, Y. J.; Erlebacher, J. Nanoporous Gold Leaf: "Ancient Technology". *Adv. Mater.* **2004**, *16*, 1897–1900.
14. Gogotsi, Y.; Simon, P. True Performance Metrics in Electrochemical Energy Storage. *Science* **2011**, *334*, 917–918.
15. Luo, J. S.; Liu, J. L.; Zeng, Z. Y.; Ng, C. F.; Ma, L. J.; Zhang, H.; Lin, J. Y.; Shen, Z. X.; Fan, H. J. Three-Dimensional Graphene Foam Supported Fe_3O_4 Lithium Battery Anodes with Long Cycle Life and High Rate Capability. *Nano Lett.* **2013**, *13*, 6136–6143.
16. Ji, J. Y.; Zhang, L. L.; Ji, H. X.; Li, Y.; Zhao, X.; Bai, X.; Fan, X. B.; Zhang, F. B.; Ruoff, R. S. Nanoporous Ni(OH) Thin Film on 3D Ultrathin-Graphite Foam for Asymmetric Supercapacitor. *ACS Nano* **2013**, *7*, 6237–6243.
17. Hou, C.; Lang, X. Y.; Han, G. F.; Li, Y. Q.; Zhao, L.; Wen, Z.; Zhu, Y. F.; Zhao, M.; Li, J. C.; Lian, J. S.; *et al.* Integrated Solid/Nanoporous Copper/Oxide Hybrid Bulk Electrodes for High-performance Lithium-Ion Batteries. *Sci. Rep.* **2013**, *3*, 2878.
18. Zhang, S. C.; Xing, Y. L.; Jiang, T.; Du, Z. J.; Li, F.; He, L.; Liu, W. B. A Three-Dimensional Tin-Coated Nanoporous Copper for Lithium-Ion Battery Anodes. *J. Power Sources* **2011**, *196*, 6915–6919.
19. Yu, Y.; Chen, C. H.; Shui, J. L.; Xie, S. Nickel-Foam-Supported Reticular CoO-Li_2O Composite Anode Materials for Lithium Ion Batteries. *Angew. Chem., Int. Ed.* **2005**, *44*, 7085–7089.
20. Wang, Z. L.; Xu, D.; Xu, J. J.; Zhang, L. L.; Zhang, X. B. Graphene Oxide Gel-Derived, Free-Standing, Hierarchically Porous Carbon for High-Capacity and High-Rate Rechargeable Li-O_2 Batteries. *Adv. Funct. Mater.* **2012**, *22*, 3699–3705.
21. Li, N.; Chen, Z. P.; Ren, W. C.; Li, F.; Cheng, H. M. Flexible Graphene-Based Lithium Ion Batteries with Ultrafast Charge and Discharge Rates. *Proc. Natl. Acad. Sci. U.S.A.* **2012**, *109*, 17360–17365.
22. Rolison, D. R.; Long, J. W.; Lytle, J. C.; Fischer, A. E.; Rhodes, C. P.; McEvoy, T. M.; Bourga, M. E.; Lubers, A. M. Multifunctional 3D Nanoarchitectures for Energy Storage and Conversion. *Chem. Soc. Rev.* **2009**, *38*, 226–252.
23. Lu, Q.; Lattanzi, M. W.; Chen, Y.; Kou, X.; Li, W.; Fan, X.; Unruh, K. M.; Chen, J. G.; Xiao, J. Q. Supercapacitor Electrodes with High-Energy and Power Densities Prepared from Monolithic NiO/Ni Nanocomposites. *Angew. Chem., Int. Ed.* **2011**, *123*, 6979–6982.
24. Wang, W.; Tian, M.; Abdulagatov, A.; George, S. M.; Lee, Y. C.; Yang, R. Three-Dimensional Ni/TiO_2 Nanowire Network for High Areal Capacity Lithium Ion Microbattery Applications. *Nano Lett.* **2012**, *12*, 655–660.
25. Chabi, S.; Peng, C.; Hu, D.; Zhu, Y. Ideal Three - Dimensional Electrode Structures for Electrochemical Energy Storage. *Adv. Mater.* **2014**, *26*, 2440–2445.
26. Cheah, S. K.; Perre, E.; Rooth, M.; Fondell, M.; Hårsta, A.; Nyholm, L.; Boman, M.; Gustafsson, T.; Lu, J.; Simon, P. Self-Supported Three-Dimensional Nanoelectrodes for Microbattery Applications. *Nano Lett.* **2009**, *9*, 3230–3233.
27. Lang, X.; Hirata, A.; Fujita, T.; Chen, M. Three-Dimensional Hierarchical Nanoporosity for Ultrahigh Power and Excellent Cyclability of Electrochemical Pseudocapacitors. *Adv. Energy Mater.* **2014**, *4*, 1301809.
28. Marichy, C.; Bechelany, M.; Pinna, N. Atomic Layer Deposition of Nanostructured Materials for Energy and Environmental Applications. *Adv. Mater.* **2012**, *24*, 1017–1032.
29. Meng, X. B.; Yang, X. Q.; Sun, X. L. Emerging Applications of Atomic Layer Deposition for Lithium-Ion Battery Studies. *Adv. Mater.* **2012**, *24*, 3589–3615.
30. Li, X. F.; Liu, J.; Banis, M. N.; Lushington, A.; Li, R. Y.; Cai, M.; Sun, X. L. Atomic Layer Deposition of Solid-State Electrolyte Coated Cathode Materials with Superior High-Voltage Cycling Behavior for Lithium Ion Battery Application. *Energy Environ. Sci.* **2014**, *7*, 768–778.
31. Ye, J. C.; An, Y. H.; Heo, T. W.; Biener, M. M.; Nikolic, R. J.; Tang, M.; Jiang, H.; Wang, Y. M. Enhanced Lithiation and Fracture Behavior of Silicon Mesoscale Pillars *via* Atomic Layer Coatings and Geometry Design. *J. Power Sources* **2014**, *248*, 447–456.
32. Gerasopoulos, K.; Pomerantseva, E.; McCarthy, M.; Brown, A.; Wang, C. S.; Culver, J.; Ghodssi, R. Hierarchical Three-Dimensional Microbattery Electrodes Combining Bottom-Up Self-Assembly and Top-Down Micromachining. *ACS Nano* **2012**, *6*, 6422–6432.
33. Bagge-Hansen, M.; Wichmann, A.; Wittstock, A.; Lee, J. R.; Ye, J.; Willey, T. M.; Kuntz, J. D.; van Buuren, T.; Biener, J.; Bäumer, M. Quantitative Phase Composition of TiO_2-Coated Nanoporous Au Monoliths by X-ray Absorption Spectroscopy and Correlations to Catalytic Behavior. *J. Phys. Chem. C* **2014**, *118*, 4078–4084.
34. Chunmei, B.; M, X.; Sun, X.; Travis, J. J.; Wang, G.; Sun, H.; Dillon, A. C; Lian, J.; Steven, M. G. Atomic Layer Deposition of Amorphous TiO_2 on Graphene as an Anode for Li-Ion Batteries. *Nanotechnology* **2013**, *24*, 424002.
35. Shin, J. Y.; Samuelis, D.; Maier, J. Sustained Lithium-Storage Performance of Hierarchical, Nanoporous Anatase TiO_2 at High Rates: Emphasis on Interfacial Storage Phenomena. *Adv. Funct. Mater.* **2011**, *21*, 3464–3472.
36. Wagemaker, M.; Borghols, W. J. H.; Mulder, F. M. Large Impact of Particle Size on Insertion Reactions. A Case for Anatase Li_xTiO_2. *J. Am. Chem. Soc.* **2007**, *129*, 4323–4327.
37. Wang, J.; Polleux, J.; Lim, J.; Dunn, B. Pseudocapacitive Contributions to Electrochemical Energy Storage in TiO_2 (Anatase) Nanoparticles. *J. Phys. Chem. C* **2007**, *111*, 14925–14931.
38. Xin, X.; Zhou, X. F.; Wu, J. H.; Yao, X. Y.; Liu, Z. P. Scalable Synthesis of TiO_2/Graphene Nanostructured Composite with High-Rate Performance for Lithium Ion Batteries. *ACS Nano* **2012**, *6*, 11035–11043.
39. Qiu, Y. C.; Yan, K. Y.; Yang, S. H.; Jin, L. M.; Deng, H.; Li, W. S. Synthesis of Size-Tunable Anatase TiO_2 Nanospindles and Their Assembly into Anatase@Titanium Oxynitride/Titanium Nitride-Graphene Nanocomposites for Rechargeable Lithium Ion Batteries with High Cycling Performance. *ACS Nano* **2010**, *4*, 6515–6526.
40. Biener, M. M.; Ye, J.; Baumann, T. F.; Wang, Y. M.; Shin, S. J.; Biener, J.; Hamza, A. V. Ultra-Strong and Low-Density Nanotubular Bulk Materials with Tunable Feature Sizes. *Adv. Mater.* **2014**, *26*, 4808–4813.
41. Lunell, S.; Stashans, A.; Ojamae, L.; Lindstrom, H.; Hagfeldt, A. Li and Na Diffusion in TiO_2 from Quantum Chemical Theory *versus* Electrochemical Experiment. *J. Am. Chem. Soc.* **1997**, *119*, 7374–7380.
42. Kim, S. W.; Han, T. H.; Kim, J.; Gwon, H.; Moon, H. S.; Kang, S. W.; Kim, S. O.; Kang, K. Fabrication and Electrochemical Characterization of TiO_2 Three-Dimensional Nanonetwork Based on Peptide Assembly. *ACS Nano* **2009**, *3*, 1085–1090.
43. Ortiz, G. F.; Hanzu, I.; Djenizian, T.; Lavela, P.; Tirado, J. L.; Knauth, P. Alternative Li-Ion Battery Electrode Based on Self-Organized Titania Nanotubes. *Chem. Mater.* **2009**, *21*, 63–67.
44. Zhang, H.; Li, G. R.; An, L. P.; Yan, T. Y.; Gao, X. P.; Zhu, H. Y. Electrochemical Lithium Storage of Titanate and Titania Nanotubes and Nanorods. *J. Phys. Chem. C* **2007**, *111*, 6143–6148.
45. Han, H.; Song, T.; Bae, J.-Y.; Nazar, L. F.; Kim, H.; Paik, U. Nitridated TiO_2 Hollow Nanofibers as an Anode Material for High Power Lithium Ion Batteries. *Energy Environ. Sci.* **2011**, *4*, 4532.
46. Saravanan, K.; Ananthanarayanan, K.; Balaya, P. Mesoporous TiO_2 with High Packing Density for Superior Lithium Storage. *Energy Environ. Sci.* **2010**, *3*, 939.
47. Vijayaraghavan, B.; Ely, D. R.; Chiang, Y.-M.; García-García, R.; García, R. E. An Analytical Method to Determine Tortuosity in Rechargeable Battery Electrodes. *J. Electrochem. Soc.* **2012**, *159*, A548–A552.
48. Vanbrake, J.; Heertjes, P. M. Analysis of Diffusion in Macroporous Media in Terms of a Porosity, a Tortuosity and a

Constrictivity Factor. *Int. J. Heat Mass Transfer* **1974**, *17*, 1093–1103.
49. Ebner, M.; Chung, D. W.; García, R. E.; Wood, V. Tortuosity Anisotropy in Lithium-Ion Battery Electrodes. *Adv. Energy Mater.* **2014**, *4*, 1301278.
50. Xue, Y.; Markmann, J.; Duan, H.; Weissmüller, J.; Huber, P. Switchable Imbibition in Nanoporous Gold. *Nat. Commun.* **2014**, *5*, 1–8.
51. Malik, R.; Zhou, F.; Ceder, G. Kinetics of Non-Equilibrium Lithium Incorporation in $LiFePO_4$. *Nat. Mater.* **2011**, *10*, 587–590.
52. Shen, L. F.; Zhang, X. G.; Li, H. S.; Yuan, C. Z.; Cao, G. Z. Design and Tailoring of a Three-Dimensional TiO_2-Graphene-Carbon Nanotube Nanocomposite for Fast Lithium Storage. *J. Phys. Chem. Lett.* **2011**, *2*, 3096–3101.
53. Yang, Z. G.; Choi, D.; Kerisit, S.; Rosso, K. M.; Wang, D. H.; Zhang, J.; Graff, G.; Liu, J. Nanostructures and Lithium Electrochemical Reactivity of Lithium Titanites and Titanium Oxides: A Review. *J. Power Sources* **2009**, *192*, 588–598.
54. Weppner, W.; Huggins, R. A. Determination of the Kinetic Parameters of Mixed-Conducting Electrodes and Application to the System Li_3Sb. *J. Electrochem. Soc.* **1977**, *124*, 1569–1578.
55. Singh, D. P.; George, A.; Kumar, R. V.; ten Elshof, J. E.; Wagemaker, M. Nanostructured TiO_2 Anatase Micropatterned Three-Dimensional Electrodes for High-Performance Li-Ion Batteries. *J. Phys. Chem. C* **2013**, *117*, 19809–19815.
56. Eustache, E.; Tilmant, P.; Morgenroth, L.; Roussel, P.; Patriarche, G.; Troadec, D.; Rolland, N.; Brousse, T.; Lethien, C. Silicon-Microtube Scaffold Decorated with Anatase TiO_2 as a Negative Electrode for a 3D Litium-Ion Microbattery. *Adv. Energy Mater.* **2014**, *4*, 1301612.
57. Simon, P.; Gogotsi, Y. Materials for Electrochemical Capacitors. *Nat. Mater.* **2008**, *7*, 845–854.
58. Mukherjee, R.; Thomas, A. V.; Krishnamurthy, A.; Koratkar, N. Photothermally Reduced Graphene as High-Power Anodes for Lithium-Ion Batteries. *ACS Nano* **2012**, *6*, 7867–7878.